

Research Paper

Refined and dynamic susceptibility assessment of landslides using InSAR and machine learning models



Yingdong Wei^a, Haijun Qiu^{a,b,*}, Zijing Liu^a, Wenchao Huangfu^a, Yaru Zhu^a, Ya Liu^a, Dongdong Yang^a, Ulrich Kamp^c

^a Shaanxi Key Laboratory of Earth Surface and Environmental Carrying Capacity, College of Urban and Environmental Sciences, Northwest University, Xi'an 710127, China

^b Institute of Earth Surface System and Hazards, College of Urban and Environmental Sciences, Northwest University, Xi'an 710127, China

^c Earth and Environmental Sciences Discipline, Department of Natural Sciences, University of Michigan-Dearborn, Dearborn, MI 48104, USA

ARTICLE INFO

Article history:

Received 20 March 2024

Revised 30 May 2024

Accepted 8 July 2024

Available online 9 July 2024

Handling Editor: Wengang Zhang

Keywords:

Landslide susceptibility

Machine learning models

InSAR

Dynamic assessment

ABSTRACT

Landslide susceptibility assessment is crucial in predicting landslide occurrence and potential risks. However, traditional methods usually emphasize on larger regions of landsliding and rely on relatively static environmental conditions, which exposes the hysteresis of landslide susceptibility assessment in refined-scale and temporal dynamic changes. This study presents an improved landslide susceptibility assessment approach by integrating machine learning models based on random forest (RF), logical regression (LR), and gradient boosting decision tree (GBDT) with interferometric synthetic aperture radar (InSAR) technology and comparing them to their respective original models. The results demonstrated that the combined approach improves prediction accuracy and reduces the false negative and false positive errors. The LR-InSAR model showed the best performance in dynamic landslide susceptibility assessment at both regional and smaller scale, particularly when identifying areas of high and very high susceptibility. Modeling results were verified using data from field investigations including unmanned aerial vehicle (UAV) flights. This study is of great significance to accurately assess dynamic landslide susceptibility and to help reduce and prevent landslide risk.

© 2024 China University of Geosciences (Beijing) and Peking University. Published by Elsevier B.V. on behalf of China University of Geosciences (Beijing). This is an open access article under the CC BY-NC-ND license (<http://creativecommons.org/licenses/by-nc-nd/4.0/>).

1. Introduction

Landslides are natural disasters widely distributed all over the world with strong destructive power (Petley, 2012; Gariano and Guzzetti, 2016; An et al., 2016). The intensification of climate change and human activities triggered an increased landslide frequency, causing heavy economic losses and casualties, and hindering social development (Froude and Petley, 2018; Zhang et al., 2022a; Qiu et al., 2024). Landslide susceptibility assessment provides a scientific basis for landslide risk management and land use planning (Fell et al., 2008; Pawluszek and Borkowski, 2017). Therefore, it is necessary to further study efficient landslide susceptibility assessment methods, identify landslide-prone areas, and adopt corresponding prevention strategies to reduce and control landslide risks.

In recent years, qualitative and quantitative methods have been used to assess landslide susceptibility. Qualitative methods are mainly heuristic models such as the expert experience method (Devara et al., 2021; Gantimurova et al., 2021). However, subjective knowledge and experience of the experts may lead to uncertainty of results (Hong, 2023). An example of a quantitative method is the physics-based model (Medina et al., 2021) that relies on a large amount of detailed data and is not suitable for larger areas (Huang et al., 2020). It is difficult for statistical models (Steger et al., 2021) to explain the relationship between landsliding and environmental factors and deal with complex nonlinear problems (Frattini et al., 2010). Deep learning models such as convolutional neural network and recurrent neural network (Yi et al., 2020; Wang et al., 2020b) often show greatly varying prediction performance and low universality (Fang et al., 2022b).

Machine learning models such as support vector machines, logistic regression models, random forests, and decision tree models (Youssef et al., 2015; Wang et al., 2020a; Fu et al., 2023) have advantages in learning the inherent law and representation level of the sample data (Dou et al., 2019). They have been successfully applied in slope stability prediction and landslide spatiotemporal

* Corresponding author at: Shaanxi Key Laboratory of Earth Surface and Environmental Carrying Capacity, College of Urban and Environmental Sciences, Northwest University, Xi'an 710127, China.

E-mail address: haijunqiu@nwu.edu.cn (H. Qiu).

susceptibility modeling, with their high accuracy and ability to effectively solve complex nonlinear problems (Zhang et al., 2022b; Kumar et al., 2023; Ren et al., 2023). However, many traditional landslide susceptibility assessment studies were usually based on long-term static data (topography, geology, hydrology) and landslide inventory maps, while the dynamic characteristic factors were often ignored, and insufficient information about dynamic landslide deformation was provided, which resulted in false negative errors (Ciampalini et al., 2016; Dai et al., 2023a). It is necessary to consider the role and effect of the dynamic characteristics in susceptibility assessment to reveal and describe landslide susceptibility risks at a more realistic regional and refined scale.

Surface deformation is a response to the dynamic characteristics of landslide displacement (Li et al., 2020). The development of InSAR technology provides an effective mean to explore the spatio-temporal deformation process of landslides from large-scale to small-scale (Crosetto et al., 2016; Ma et al., 2021). Multi-temporal InSAR techniques like Pixel offset tracking (POT) (Raucoules et al., 2013), Small Baseline Subset InSAR (SBAS-InSAR) (Novellino et al., 2020), and Permanent Scatterers InSAR (PS-InSAR) (Ferretti et al., 2001) can track landslide displacement with centimeter-to-millimeter accuracy, and are widely used in real-time landslide monitoring, susceptibility mapping, and warning (Dong et al., 2018; Ma et al., 2019; Solari et al., 2020). Deformation results introduced by InSAR technology make up for the deficiency in susceptibility modeling performance of quantitative models when analyzing landslide dynamics characteristics (Novellino et al., 2021; Zhou et al., 2022; Yao et al., 2023a). Some previous studies also focused on the recognition of deformation information of InSAR technology as an evaluation and test of susceptibility results, and the two were not deeply integrated (Xie et al., 2017; Hussain et al., 2021). This study incorporated the InSAR deformation rate into our landslide susceptibility assessment and combined it with the initial susceptibility assessment results through matrix method to obtain the improved landslide susceptibility maps, instead of simply overlapping and visually comparing landslide susceptibility maps and deformation rate maps to judge whether high susceptibility areas correspond to deformation areas. In addition, some studies focused on the overall evaluation of the region while ignoring the refined small-scale area, verification methods that are more dependent on relevant evaluation indicators and optical remote sensing images, and the application of multi-source verification data are insufficient. Therefore, the combination of machine learning models and InSAR technology provides a reference for achieving a dynamic and refined susceptibility assessment and diversification of validation means.

In this study, we used machine learning models to conduct a preliminary landslide susceptibility mapping and InSAR technology to extract the surface deformation rate in exploring the dynamic landslide susceptibility assessment approach according to the assessment matrix. The objectives of this study are: (i) to improve and update initial landslide susceptibility maps, (ii) to reveal enhanced susceptibility areas and refine-analyze the evolution of small-scale typical landslides, and (iii) to conduct quantitative validation and field investigation of landslide susceptibility assessment results. The research provides a new idea for regional dynamic landslide susceptibility assessment and refined evaluation.

2. Study area and datasets

Hualong County, located in the east of Qinghai Province in China lies in the transition zone between the Qinghai-Tibet Plateau and

the Loess Plateau (Fig. 1a). The terrain is dominated by basins and valleys, and the topographic features of steep slopes, alternating ridges, and deep gullies in combination with strong uplift and regional tectonic movement create conditions for geological hazards (Yao et al., 2012; Yang et al., 2023a). The climate is continental semi-arid with a high annual temperature amplitude and a mean annual temperature of 2.2 °C. The mean annual precipitation amounts to 470 mm with a rainy season from June to September; precipitation decreases from north to south (Ma et al., 2023). Lijiaxia reservoir is in the upper reaches of the mainstem of the Yellow River, which flows from west to east in the southwest of the county. The study area is prone to landsliding in light of environmental conditions such as dense tributary network, high water volumes and flow velocities, large drop, fluvial erosion, and precipitation. Fig. 1b shows the distribution of landslides in Hualong County.

Using historical records, field survey data, and visual interpretation of Google Earth satellite images, an inventory including 394 landslides was generated (Fig. 1b). The uneven distribution of landslides across the region may be related to varying complex geological and other environmental conditions. An equal number of non-landslide locations was randomly selected to build a reference inventory for comparison reasons. The type label of the landslide locations was set to 1, while it was set to 0 for the non-landslide locations. Of all locations, 70% were used for training the model, and 30% were used for model validation (Youssef et al., 2023; Zhao et al., 2023).

Selecting appropriate landslide-conditioned reflex factors is the premise of susceptibility assessment. However, no uniform standard exists for selecting the right factors (Ayalew and Yamagishi, 2005; Reichenbach et al., 2018). Based on topography, geology, landslide distribution, and existing literature on the study area (Shi et al., 2019; Du et al., 2023), we decided for the following five underlying reflex factors: topography, land cover, geology, hydrology, and human activities. For our landslide susceptibility assessment system, we identified twelve reflex factors that effect landsliding: lithology, rainfall, elevation, slope, aspect, slope curvature, distance from river, distance from road, distance from fault, Terrain Wetness Index (TWI), landuse, and Normalized Difference Vegetation Index (NDVI) (Fig. 2). The geological map was digitized to obtain lithology and distance from faults, and all raster data were resampled to 30 m resolution; elevation, slope, aspect, curvature, and terrain wetness index were derived from the SRTM DEM with 30 m resolution; annual average rainfall data with 30 m resolution were acquired from the Fine Resolution Mapping of Mountain environment (FRMM) of the Institute of Mountain Hazards and Environment, Chinese Academy of Sciences (CAS); NDVI was extracted from the Geospatial Data Cloud (<https://www.gscloud.cn>); river network data were downloaded from the National Catalogue Service for Geographic Information (<https://www.webmap.cn>); road data were downloaded from the Open Street Map (<https://www.openstreetmap.org>).

3. Methodology

3.1. Multicollinearity analysis

Multicollinearity analysis is used to estimate the correlation between explanatory variables. To avoid impacts on model accuracy, this study used the variance inflation factor (VIF) and tolerance (TOL) to evaluate the multicollinearity among variables (Gupta and Shukla, 2023). VIF and TOL are calculated using Eqs. (1) and (2):

$$VIF = \frac{1}{1 - R_i^2} \quad (1)$$

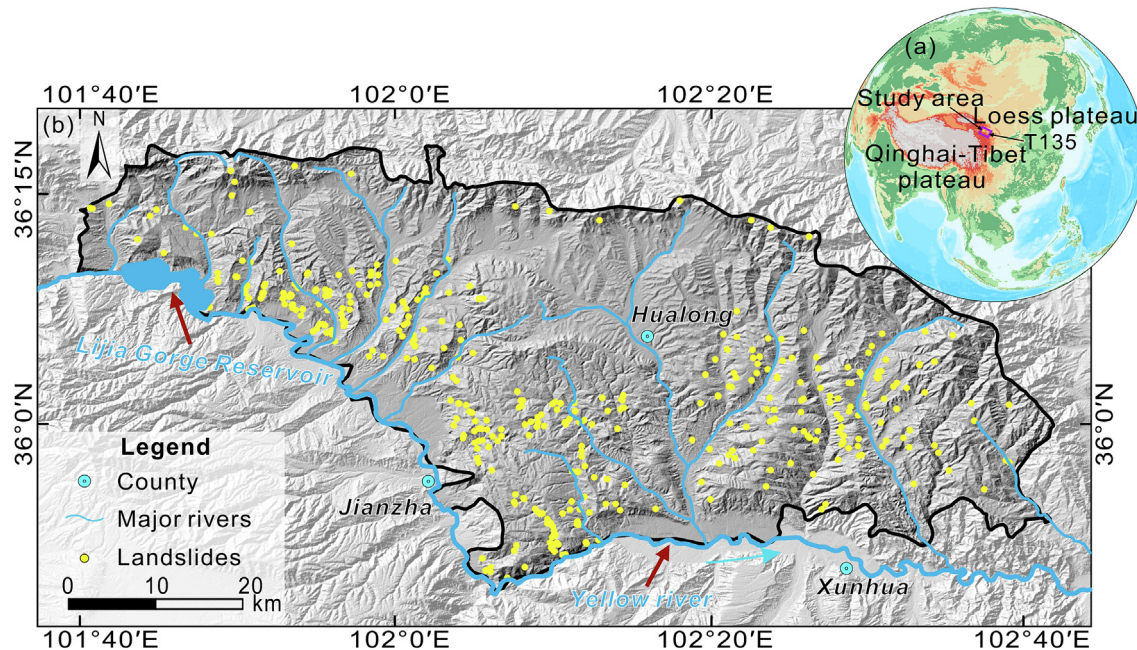


Fig. 1. The geographical location of the study area. (a) Location of the study area in the transition zone between the Qinghai-Tibet Plateau and the Loess Plateau in China. (b) Distribution of the landslide in Hualong County.

$$TOL = \frac{1}{VIF} \quad (2)$$

where, R_i^2 is the determination coefficient of the independent variable i in the regression model with other predictors; when $VIF > 10$ and $TOL < 0.1$, a high multicollinearity problem exists between the variables, they should be removed from the susceptibility modeling (Li and Hong, 2023).

3.2. Evaluation models

3.2.1. Random forest

Random Forest (RF) is an integrated machine learning algorithm for decision tree-based classifiers (Breiman, 2001), where a bootstrap method is used to generate a training set, and then multiple classification and regression trees are constructed for the sample set. When the internal nodes of each classification and regression tree split, the feature set is randomly sampled once, each node is divided using the best segmentation between the subsets of the predictor, and the optimal selection is made in the extracted feature set. Finally, the output of each classifier is combined by means or voting, which is a way to find useful but hidden patterns in a large amount of data (Kohestani et al., 2015). Owing to the randomness of the RF in selecting samples and features, it is trained by bagging and guided aggregation, which makes the RF resistant to overtraining and overfitting, resulting in a strong tolerance for outliers and noise as well as an improvement of prediction accuracy of the RF model (Zhang et al., 2021).

3.2.2. Logistic regression

Logistic regression (LR) uses logic functions to model the relationship between binary (landslide or non-landslide) and independent variables (Baharvand et al., 2020). The factors influencing landslides were defined as the independent variables, while landslide and non-landslide areas were assigned as the dependent variables. To predict the occurrence of slope failure, the optimal fitting algorithm must be found to evaluate the spatial correlation between landslide occurrence and influencing factors to effectively address the problem of facing dichotomy variables in the landslide

susceptibility assessment (Liu et al., 2022b). LR is calculated using Eq. (3):

$$P = \frac{1}{1 + e^{-(\beta_0 + \beta_1 x_1 + \beta_2 x_2 + \dots + \beta_n x_n)}} \quad (3)$$

where P is the probability of landslide occurrence, β_1, \dots, β_n represent the logistic regression coefficient, β_0 is the intercept of the logistic regression equation, e is the natural constant, x_1, x_2, \dots , and x_n represents the predictive variable of landslide influencing factors.

3.2.3. Gradient boosting decision tree

Gradient Boosting Decision Tree (GBDT) is a model based on regression tree and gradient iteration, which adopts a linear combination of the primary function and continuously reduces residuals generated during the training process to classify the regression data (Friedman, 2001). It mainly generates a weak classifier through multiple iterations, where the classifier of each iteration step is trained based on the residual of the previous round of classifiers. Each iteration takes the current prediction as the basis, and the next weak classifier fits the residual of the error function to the predicted value. Finally, the predicted value of all classifiers is synthesized to produce the final prediction result. (Jiang et al., 2023). GBDT can be used for both classification and regression problems. It can flexibly deal with various types of data, including continuous and discrete values, and it has a good generalization ability, which is relatively suitable for low-dimensional data (Liang et al., 2021).

3.3. Dynamic susceptibility mapping with integrated InSAR technology

Small Baseline Subset Interferometric Synthetic Aperture Radar (SBAS-InSAR) technology can overcome the disadvantages of conventional differential interferometry technology because the deformation measurement error is small, which improves the reliability of monitoring results (Berardino et al., 2002; Hooper, 2008). Compared with other multi-temporal InSAR techniques, SBAS-InSAR is more suitable for mountain environments, and it easily calculates

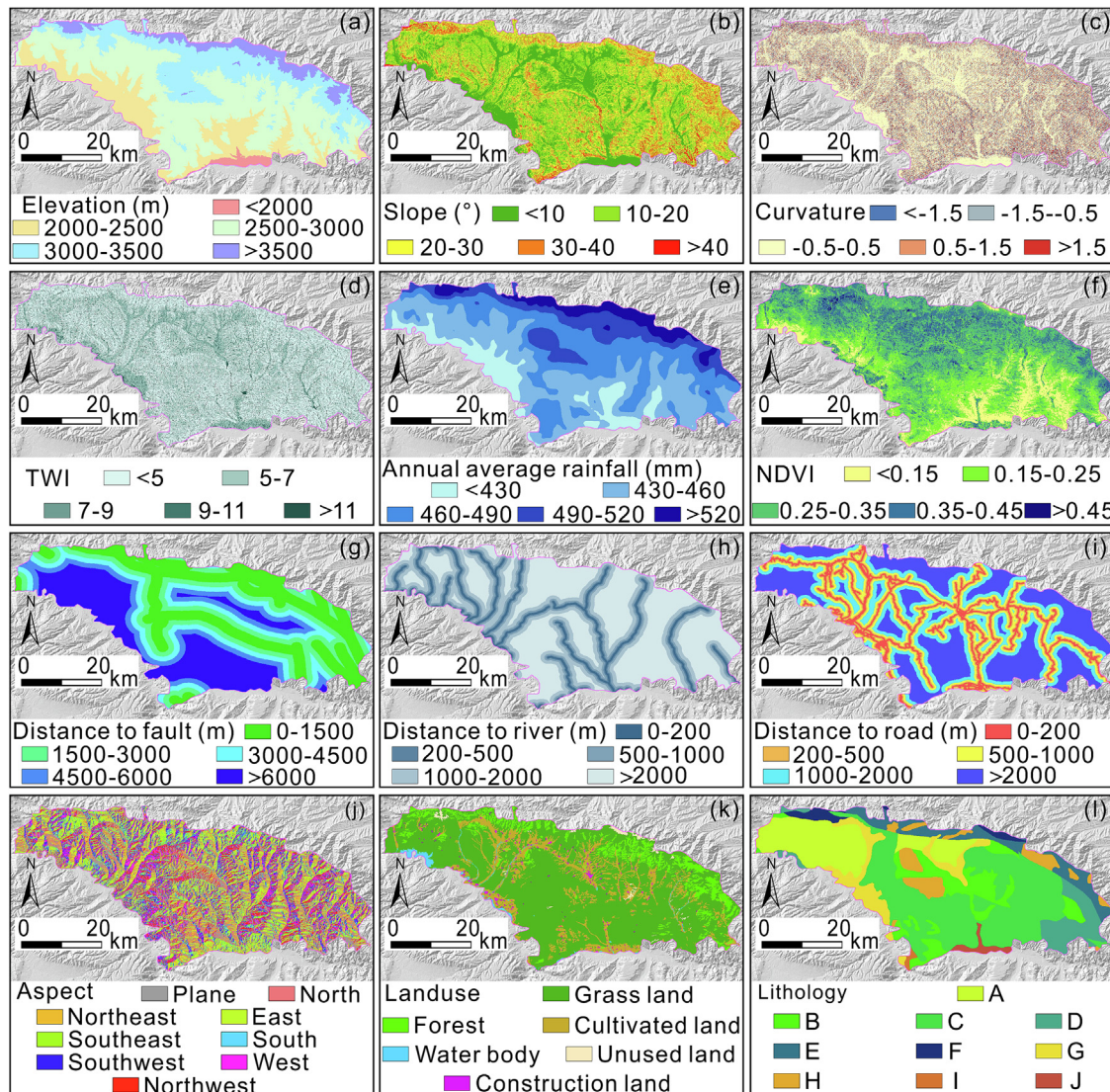


Fig. 2. The twelve reflex factors that effect landsliding selected in this study.

the annual dynamic surface deformation rate of landslides (Yang et al., 2023b).

Following the small baseline principle, we collected 80 images taken during a descending orbit along satellite track 135 from 24 October 2019 to 26 September 2022, with an incidence angle of 41.78° and a spatial resolution of $14\text{ m} \times 2\text{ m}$. From this data set, 334 interference pairs were generated. POD precision orbit ephemerides were used to remove orbital errors, and the Space Shuttle Radar Topography Mission Digital Elevation Model (SRTM DEM, 30 m-resolution) was used for image registration and terrain phase removal (Ye et al., 2024). The slow-lose correlation filtering phase pixels are identified based on the average spatial coherence (Shahzad et al., 2020). Phase unwinding was performed by using the Minimum Cost Flow method (MCF), and displacement and deformation parameters were estimated using the Singular Value Decomposition (SVD) and least square methods (Liu et al., 2024) to solve the phase sequence of a single main image. Finally, spatiotemporal filtering was used to estimate and remove the atmospheric delay phase to obtain the deformation velocity and time series of the coherent target (Morishita et al., 2020).

To obtain regional and small-scale dynamic assessment results, information on landslide deformation is introduced to correct the

inappropriate zoning of the initial landslide susceptibility maps, which can further reduce the interference of susceptibility results caused by ignoring dynamic factors. Following Dai et al. (2023b), this study adopted machine learning models and InSAR technology to obtain preliminary susceptibility and surface deformation rate, and the results were uniformly normalized. Considering the average velocity in each cell, the natural breaks method was used to divide the surface deformation rate obtained by SBAS-InSAR into five levels (Yao et al., 2023b). The higher the level, the greater the susceptibility level and deformation rate. The preliminary landslide susceptibility map was updated using an evaluation matrix as shown in Table 1.

3.4. Model validation

Confusion matrix parameters, sensitivity, specificity, and overall accuracy help to evaluate performance of different classifiers (Al-Abadi and Al-Najar, 2019; Liu et al., 2023b), where true positive (TP) indicates correct and false positive (FP) indicates incorrect classification of landslide samples, while false negative (FN) indicates correct and true negative (TN) indicates incorrect classification of non-landslide samples. The overall accuracy (OA)

Table 1

The combination matrix of landslide susceptibility and deformation rate. S1-S5 represent preliminary susceptibility levels from very low to very high, while V1-V5 represent deformation levels from low to high.

Level	S1	S2	S3	S4	S5
V1	1	1	1	2	3
V2	1	2	2	3	4
V3	1	2	3	4	5
V4	2	3	4	4	5
V5	3	4	5	5	5

represents the proportion of the total samples that was correctly predicted. Sensitivity (TPR) refers to the proportion of correctly classified landslide samples, while specificity (TNR) refers to the proportion of correctly classified non-landslide samples (Pham et al., 2018). TPR and TNR range from 0 to 1, with increasing quality of the model output, as described by Eqs. (4)-(6):

$$\text{Sensitivity} = \frac{TP}{TP + FN} \quad (4)$$

$$\text{Specificity} = \frac{TN}{FP + TN} \quad (5)$$

$$OA = \frac{TP + TN}{TP + FP + TN + FN} \quad (6)$$

4. Results

4.1. Collinearity analysis of landslide-influencing factors

The maximum VIF was 5.033, and the minimum TOL was 0.199; the VIF and TOL values of all factors are within a reasonable range of intervals ($VIF < 10$ and $TOL > 0.1$) (Table 2). This means that the twelve landslide-influencing factors do not have multicollinearity problems, which ensures accuracy in the subsequent susceptibility modeling.

4.2. Surface deformation rate acquired by SBAS-InSAR

The average surface deformation rate in the LOS direction obtained by the SBAS-InSAR method is shown in Fig. 3. Negative red values indicate that the surface target is moving away from the satellite in the LOS direction, while positive blue values indicate that the surface target is moving closer to the satellite in the LOS direction. Areas of zero deformation occur because of external disturbances such as vegetation and noise during the processing of InSAR, which is interpolated to fully integrate with the susceptibil-

Table 2
VIF and tolerance statistics of predisposing factors.

Predisposing factor	VIF	TOL
Elevation	3.838	0.261
Slope	1.516	0.66
Aspect	1.178	0.849
Curvature	1.354	0.738
NDVI	1.276	0.784
Rainfall	5.033	0.199
Lithology	1.888	0.53
TWI	1.621	0.617
Distance to river	1.256	0.796
Distance to road	1.358	0.737
Distance to fault	1.835	0.545
Landuse	1.374	0.728

ity. Fig. 3a shows that the average annual deformation rate ranged from -135 to 145 mm/yr. The area of severe deformation was distributed across the south, while areas of large deformation were mainly concentrated in the western and eastern regions. The deformation rate had a standard deviation of 6.96 mm/yr and showed a normal distribution (Fig. 3b), indicating that the area remained basically stable.

4.3. Landslide susceptibility mapping

Landslide susceptibility modeling was conducted based on RF, RF-InSAR, LR, LR-InSAR, GBDT and GBDT-InSAR models. The Jenks natural breaks method can identify the best grouping similarity value and maximize the difference between classes, which has high applicability in landslide susceptibility map classification (Jenks, 1967; Arabameri et al., 2020). Using the natural breaks method in ArcGIS 10.2 software, the susceptibility maps were divided into five grades: very low, low, moderate, high, and very high (Liu et al., 2023c; Sharma et al., 2024). Fig. 4 illustrates the landslide susceptibility mapping results from these different models, with bright red representing areas of very high susceptibility and bright green representing areas of very low susceptibility. In general, the landslide susceptibility classification using the combined machine learning-InSAR model presents a similar spatial distribution as the preliminary susceptibility map. The very high and high susceptibility areas were distributed mainly across the southwest, southcentral, and southeastern regions as well as on both sides along the river. In contrast, the very low and low susceptibility areas were mainly distributed across the central and northern regions in proximity to towns. The northern region is dominated by higher mountains and has only few rivers, and human activities are rare. If a model predicts more landslides in the high and very high susceptibility zones, more disaster hazards will be discovered and identified (Huang et al., 2022; Chang et al., 2023). Indeed, compared with the original model, the combined machine learning-InSAR models predicted more landslide area and number in the very high and high susceptibility regions (Table 3), which also means that more high-risk landslides were detected, reducing underreporting and neglect of disaster hazards, reflecting a more satisfactory prediction performance.

4.4. Model validation and comparison

The confusion matrix calculates the relevant indicators. Fig. 5 presents the performance of the different models. When assessing the prediction of landslides in the vertical direction, the accuracy increased by 2% from RF to RF-InSAR and by 6% from LR to LR-InSAR, while it remained almost unchanged from GBDT to GBDT-InSAR. When assessing the prediction of non-landslide areas in the vertical direction, accuracy increased by 2% from RF to RF-InSAR, by 3% from LR to LR-InSAR, and by 2% from GBDT to GBDT-InSAR. The overall accuracy increased by 2% from RF to RF-InSAR, by 4% from LR to LR-InSAR, and by 2% from GBDT to GBDT-InSAR. These results demonstrate that RF-InSAR, LR-InSAR, and GBDT-InSAR improved the spatial prediction ability of landslide susceptibility when compared with traditional models and reduced false negative and false positive errors. When assessing the prediction of landslides in the horizontal direction, the accuracy of LR-InSAR was 10% higher than that of RF-InSAR and 9% higher than that of GBDT-InSAR. When assessing the prediction of non-landslide area, accuracy of LR-InSAR was 3% higher than that of RF-InSAR and 5% higher than that of GBDT-InSAR. The overall accuracy of LR-InSAR was the highest among the three models, reaching 82%. In summary, machine learning models combined with InSAR have good accuracy and prediction ability, and they can be applied to the estimation of landslide susceptibility.

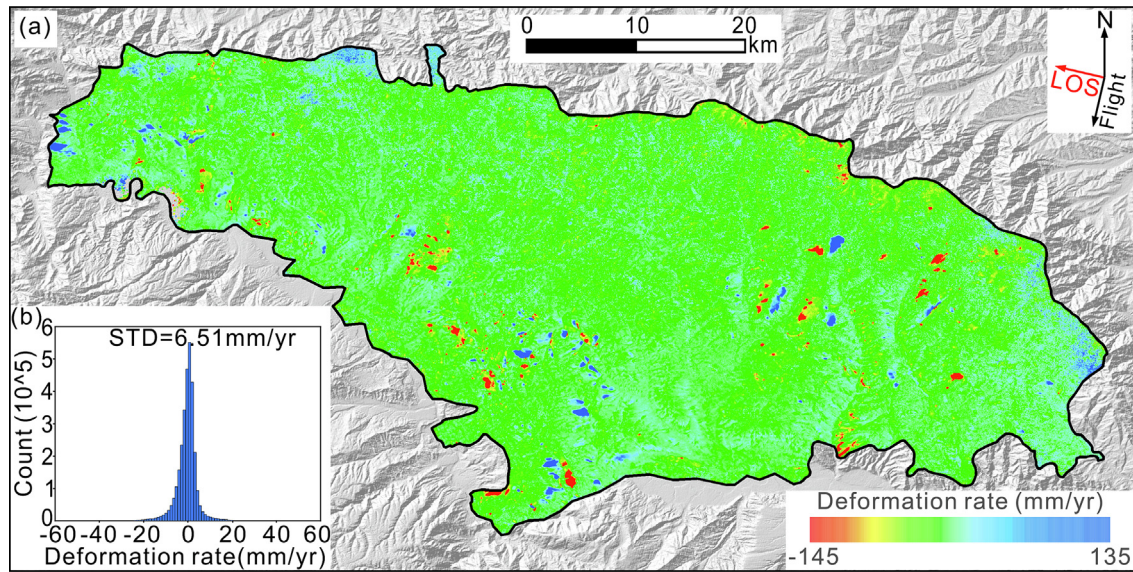


Fig. 3. Annual deformation rate in the study region obtained from SBAS-InSAR. (a) Average LOS deformation velocity map. (b) Distribution rate frequency and standard deviation.

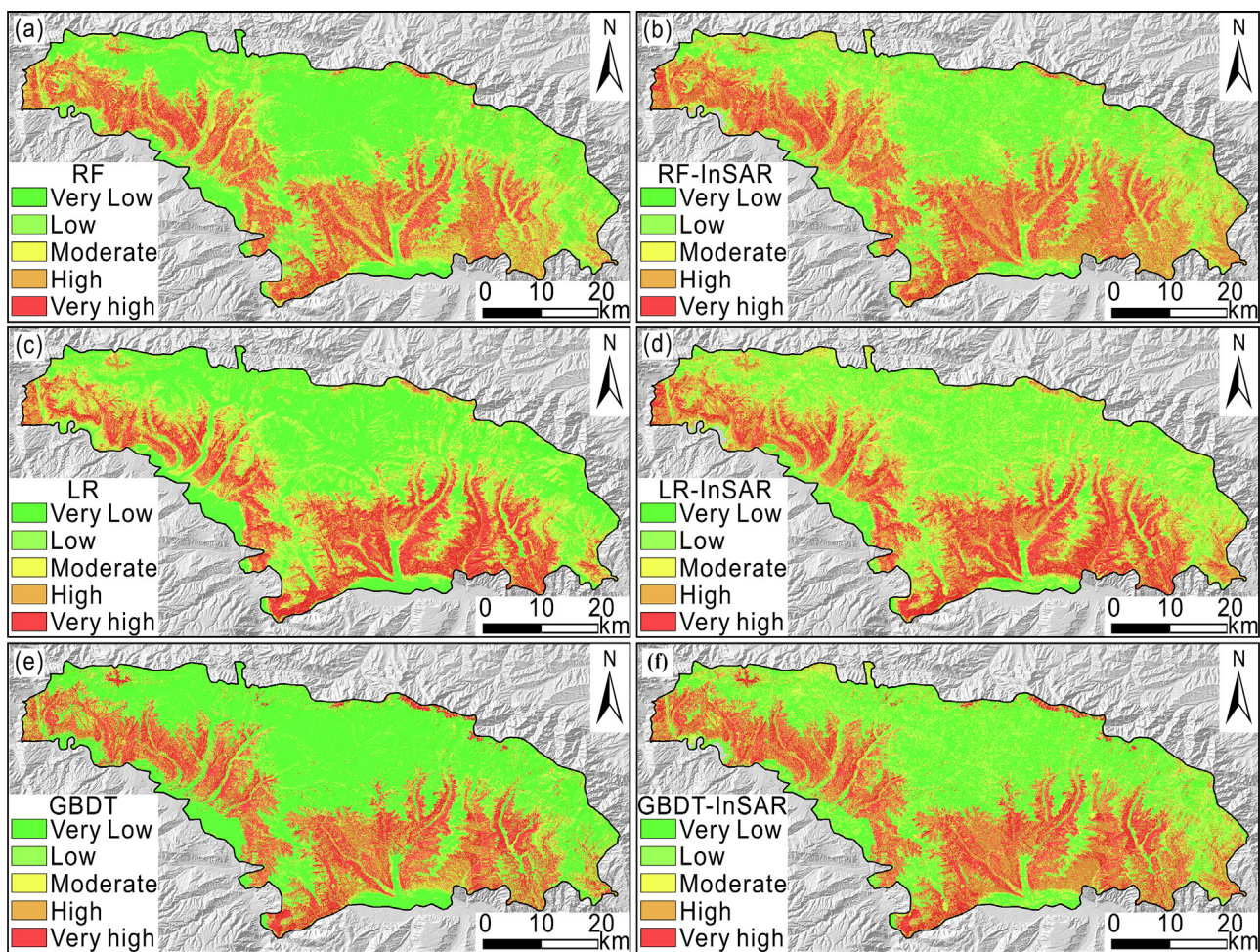
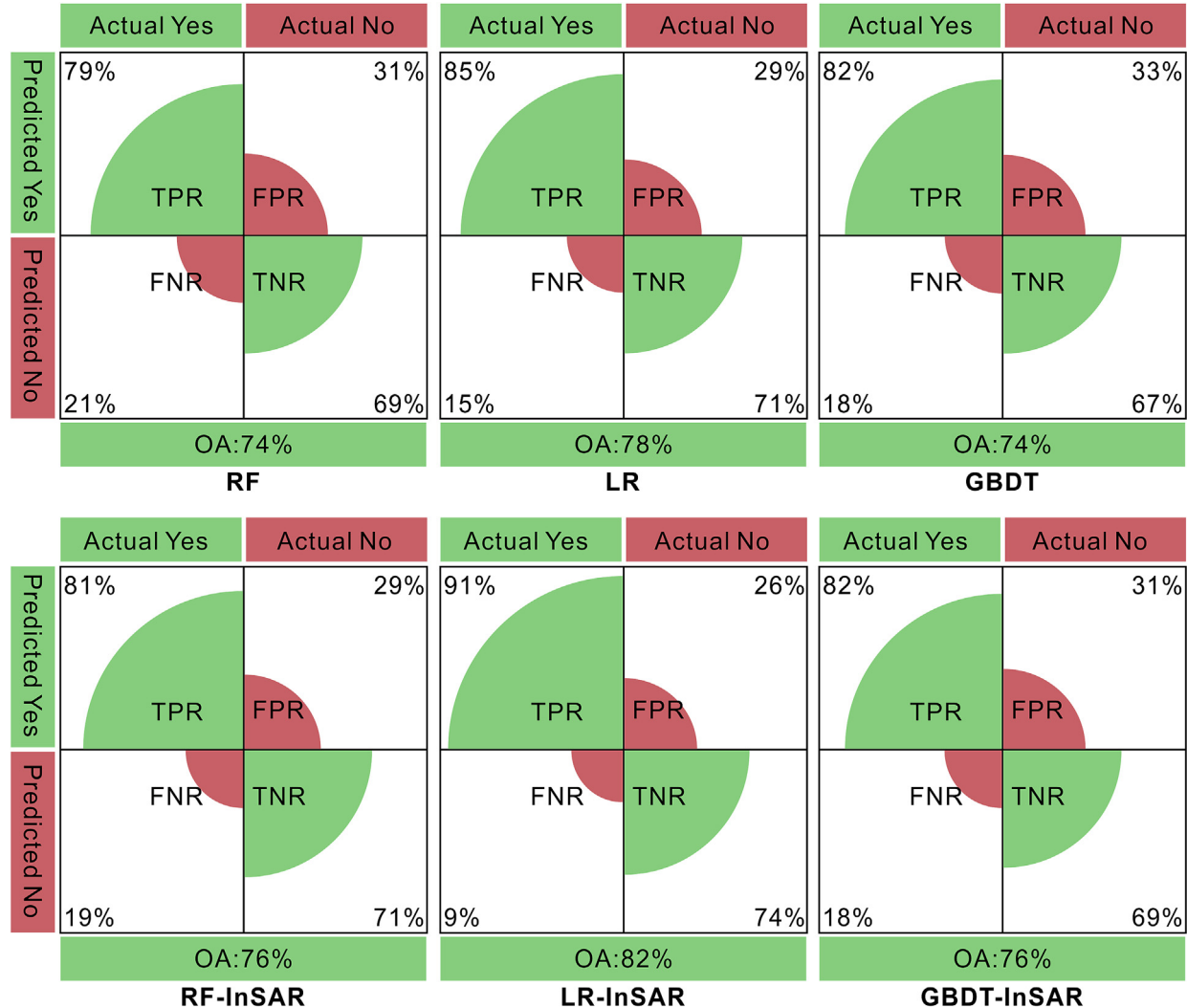


Fig. 4. Landslide susceptibility maps retrieved from different models. (a,c,e) Preliminary results. (b,d,f) Results using a combination of the original model and InSAR.

Table 3

Proportion of landslide area and number in the very high and high susceptibility classes.

Proportion (%)	Models					
	RF	RF-InSAR	LR	LR-InSAR	GBDT	GBDT-InSAR
Area	64.01	67.53	63.84	69.13	68.20	68.73
Number	75.63	80.67	84.87	90.75	77.31	82.35

**Fig. 5.** Performance of different susceptibility models evaluated by confusion matrix and overall accuracy.

4.5. Refinement analysis

4.5.1. Landslide identification in areas of increased susceptibility

The improved susceptibility assessment using InSAR can detect higher susceptibility areas. The comparison of the different models illustrates that LR-InSAR performed best in landslide prediction accuracy (Fig. 5). Using results from LR and LR-InSAR modeling, we conducted refined-scale detection on the basis of regional scale and identified three representative regions A, B, and C of enhanced susceptibility and four landslides L1-4 (Fig. 6). The susceptibility of L1 in region A changed from moderate to high, while the portion of areas of a very high susceptibility increased significantly across L2, L3, and L4 regions B and C.

4.5.2. Field verification and analysis of landslide deformation

The phenomenon of landslide damage is an intuitive reflection of landslide susceptibility (Cao et al., 2022). To further verify the results of our landslide susceptibility mapping, field investigations including UAV flights were conducted. The characteristics of landslide deformation and their relationship with the induced factors were analyzed to confirm the cause of deformation.

L1 is a loess landslide with a tongue shape and a main southeast orientation. Long gullies run downslope along its edges (Fig. 7b, c) and a secondary scarp developed in its lower part (Fig. 7b). The failure tilted or destroyed several power poles (Fig. 7d), and the right section of its bottom was eroded by the river (Fig. 7d). Construction activities could be observed near the landslide (Fig. 7e), and man-

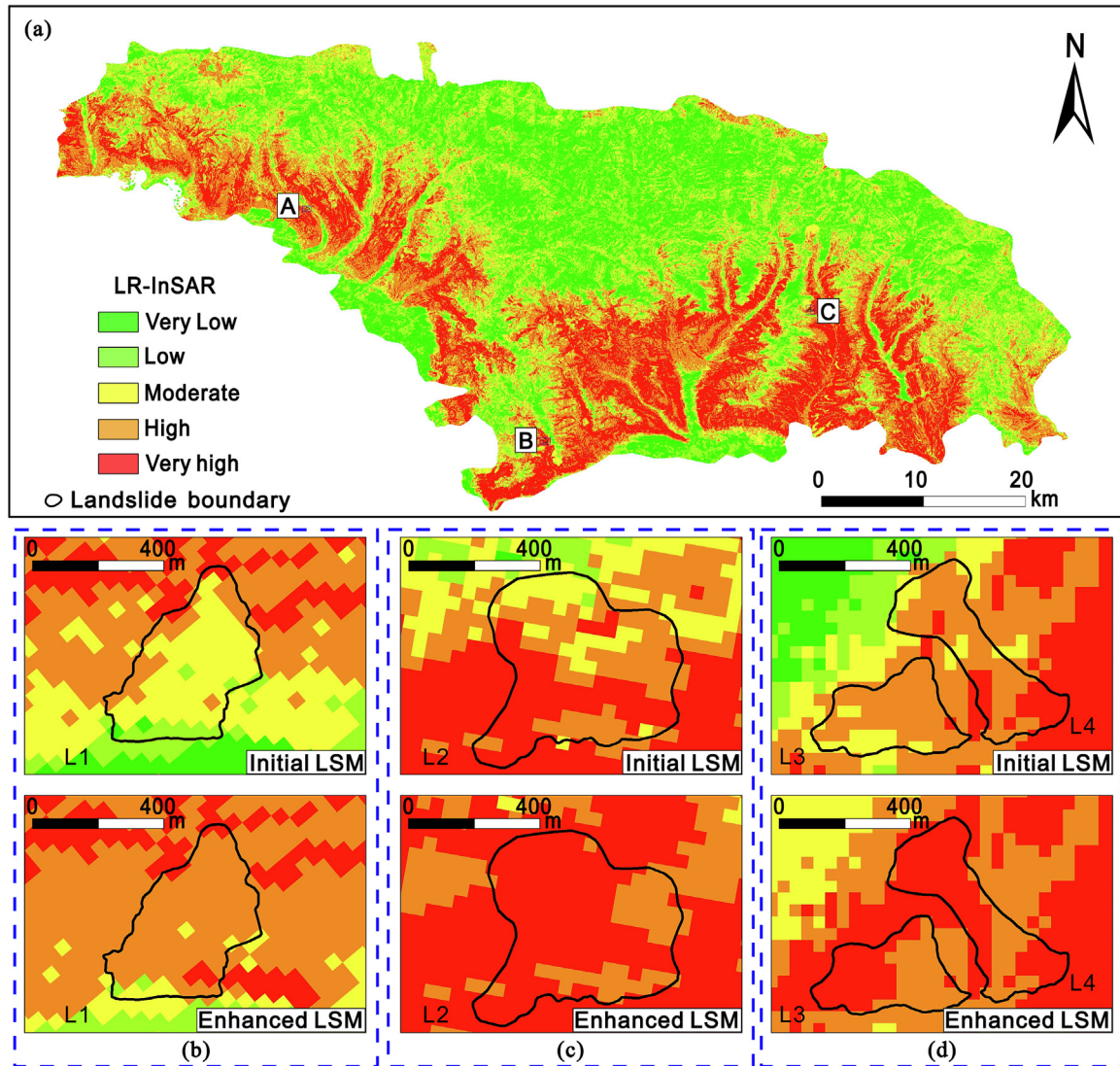


Fig. 6. Susceptibility enhancement and landslide identification of representative regions. (a) Refined-scale detection on the basis of regional scale. (b)-(d) Upper row represents the preliminary susceptibility results using the LR model, while the lower row represents the results using the improved LR-InSAR model corresponding to A, B, and C regions.

ual digging had happened at its bottom. This indicated that L1 landslide have high susceptibility characteristic, which is consistent with the results of the coupled models.

The average annual deformation rates across the landslide document that deformation occurred mainly in the landslide's lower part, while its upper part was in a stable state; the maximum deformation of up to 45 mm occurred on the right side at the landslide bottom. The overall landsliding pattern is characterized by traction. The fluvial erosion and human digging at the bottom of the landslide increased the sliding process and as such instability. To explore the temporal deformation characteristics of the landslide, four points P1-4 were selected in its upper, middle, lower, and bottom sections (Fig. 7a). By comparing the annual variations in landslide deformation and air temperature between October 2019 and July 2022, two opposite cycles were identified: while air temperature increased in the summer and decreased in the winter, deformation decreased in the summer and increased in the winter (Fig. 7f). In other words: landslide deformation was more severe during the colder winter months because it is affected by the seasonal freeze-thaw cycle.

We investigated landslide L2 using field observations and UAV imagery (Fig. 8). The surface of this ancient landslide has numerous fissures and sinkholes, and a deep gully runs along the landslide's left edge. Its right section has a stepped surface with larger vertical offsets of > 1 m. Fluvial erosion resulted in slope collapse, which eventually blocked the river and cut it off from the Yellow River. L2 landslide suffered severe damage and exhibited very high susceptibility.

To analyze the spatiotemporal deformation, we focused on the cumulative LOS deformation at L2. Fig. 9 shows that the upper rear edge began to deform first, while no significant deformation was observed in the middle and lower sections until 3 May 2020. Then, from 11 November 2020 to 26 September 2022, the deformation area gradually expanded downslope, while the right and bottom sections remained relatively stable. The deformation was always more severe in the middle and upper sections than in the lower section. P1-2 were selected for the cumulative deformation time series analysis between October 2019 and July 2022, and the impact of rainfall was qualitatively described. The cumulative deformation was 210 mm at P1, 151 mm at P2 at the rear edge.

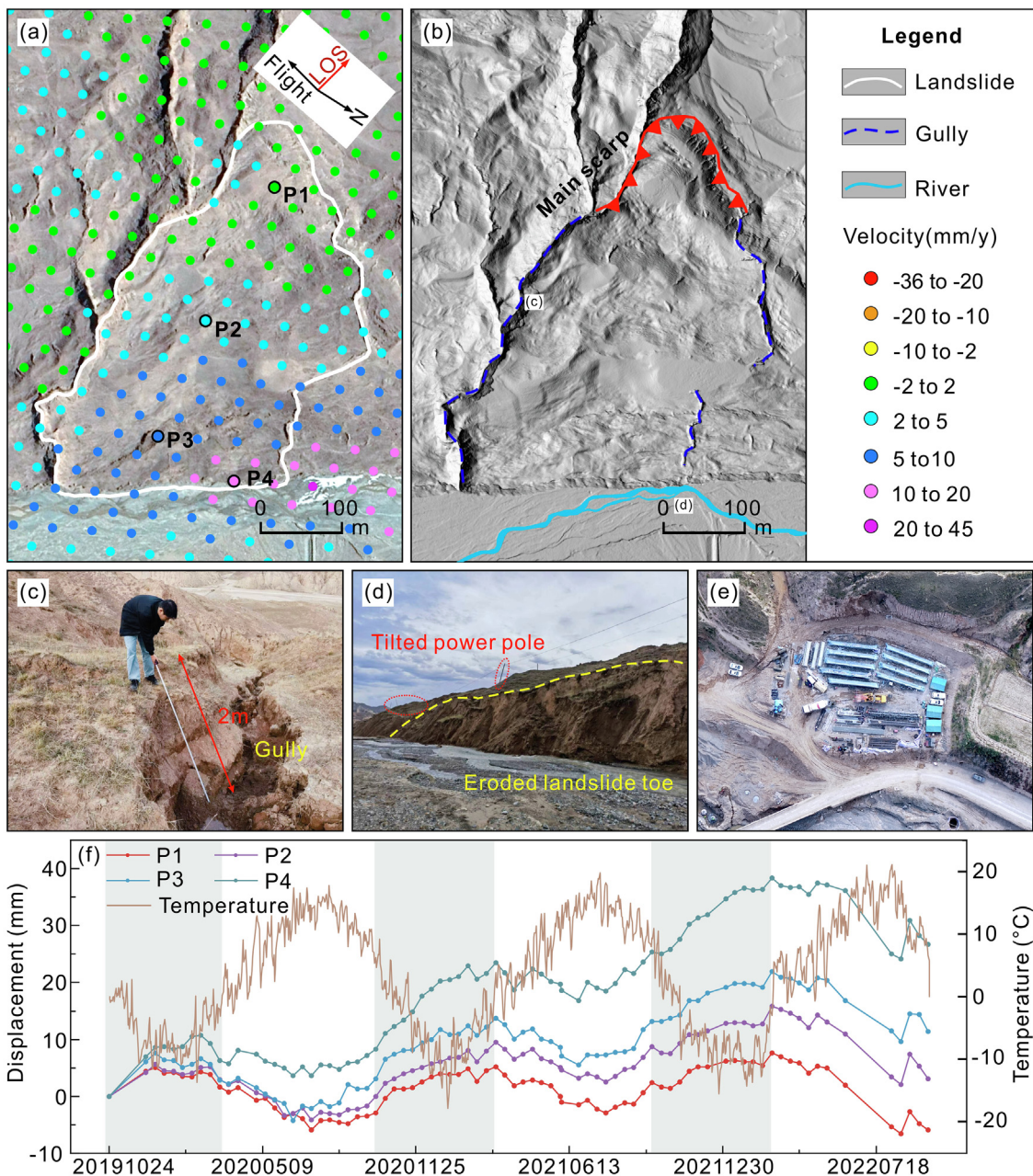


Fig. 7. Deformation at landslide L1. (a) LOS mean annual deformation rate. P1-P4 are time series points at different locations across the landslide. (b) Airborne LiDAR –based hillshade image. (c) Deep gully at the edge of the landslide. (d) Tilted power pole and eroded landslide base. (e) Engineering activities near the landslide. (f) Time series deformation curves for P1-P4 and air temperature. The grey area represents the time when displacement increases.

Fig. 9i shows that cumulative deformation increased over time at P1-P2, while the increase was the strongest at P1 at the rear edge of the landslide, weakening in downslope direction towards P2. Deformation fluctuated with the variation of rainfall during the rainy season, when the upper slope sections lost their stability first followed by the middle and lower sections that gradually deformed with an increase in cumulative displacement and compression. The numerous sinkholes, and gullies were probably a consequence of rainfall. The deformation of L2 landslide was also mainly caused by rainfall, showing the characteristics of seasonal variation.

The results from our field investigations at landslides L3 and L4 are shown in **Fig. 10**. The most significant feature of these ancient landslides are the longer gullies that reach almost along the entire longitudinal slope profile to the bottom. Numerous fissures can be

seen in the lower and bottom sections of L3 as well as in the middle and lower sections of L4. Vertical offsets and sinkholes were found in the upper section of L3. Several depressions formed in both L3 and L4, acting as main collectors of water transported through the gullies. The landslides have been severely damaged, reaching the high and very high susceptibility level, which may pose a risk of reactivation.

The cumulative deformation at L3 and L4 as well as the four monitoring locations P1-P4 are shown in **Fig. 11**. We found that only the upper left edge of L3 had a relatively large deformation of 140 mm, although the cumulative deformation in the right bottom section was only 20 mm. The cumulative deformation extended to the middle section that was relatively stable. However, from 24 October 2019 to 26 September 2022, the cumulative

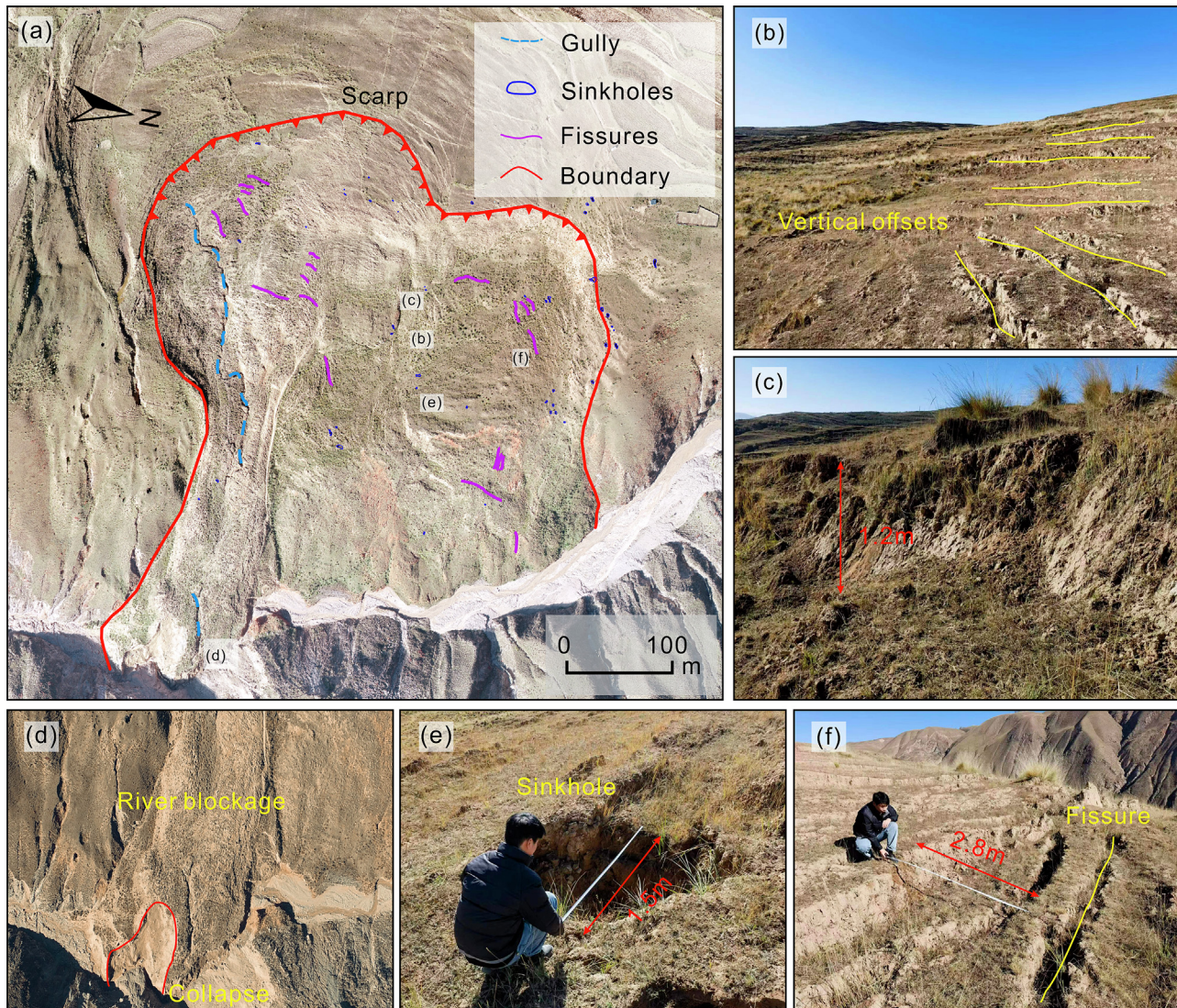


Fig. 8. Field investigations at landslide L2. (a) UAV panoramic image. (b, c) Stepped landslide surface with vertical offsets. (d) Fluvial erosion led to landslide collapse and river blockage. (e) Sinkhole. (f) Fissures.

deformation at L4 gradually increased, when the rear edge and bottom first showed signs of instability, and the deformation gradually increased from the top and bottom towards the middle section. The analysis of daily data revealed that rainfall had a significant correlation with the deformation at L3 and L4 during the rainy season (Fig. 11i). These ancient landslides underwent significant deformation under the combined effects of rainfall and their own gravity.

5. Discussion

5.1. InSAR technology in landslide susceptibility assessment

InSAR technology enhances landslide prediction accuracy of conventional machine learning models by improving the unreasonable partition of landslide susceptibility and reducing the error in probabilistic susceptibility classifications for larger regions as well as smaller-scale areas (Fig. 5). Our InSAR-improved approach successfully detected areas of enhanced susceptibility as well as landslides with high and very high susceptibility in the eastern,

central, and western parts of the study region (Fig. 6a-d), which shows it can achieve reliable susceptibility assessments in different spatial positions and reduce the impact of spatial heterogeneity (Sun et al., 2023). In contrast, the preliminary landslide assessment model was not able to accurately reflect the actual state of landslide susceptibility, for example, Fig. 6b displays landslide L1 falsely as an area of moderate and low susceptibility. After our model correction, the susceptibility level was raised to high. Due to the improvement and rectification of susceptibility, we discovered and outlined the L1 landslide. We also ascertained the cause of landslide deformation and the exactitude of susceptibility results through on-site verification (Fig. 7). The improved model is effective in accurate landslide identification and prediction, and the dynamic susceptibility assessment for a certain period is more in line with reality. This not only helps decision-makers to accurately locate highly susceptibility landslide areas and identify related hazards, but also has important practical significance for taking timely governance measures to improve risk management efficiency and disaster precaution and mitigation (Shan et al., 2023).

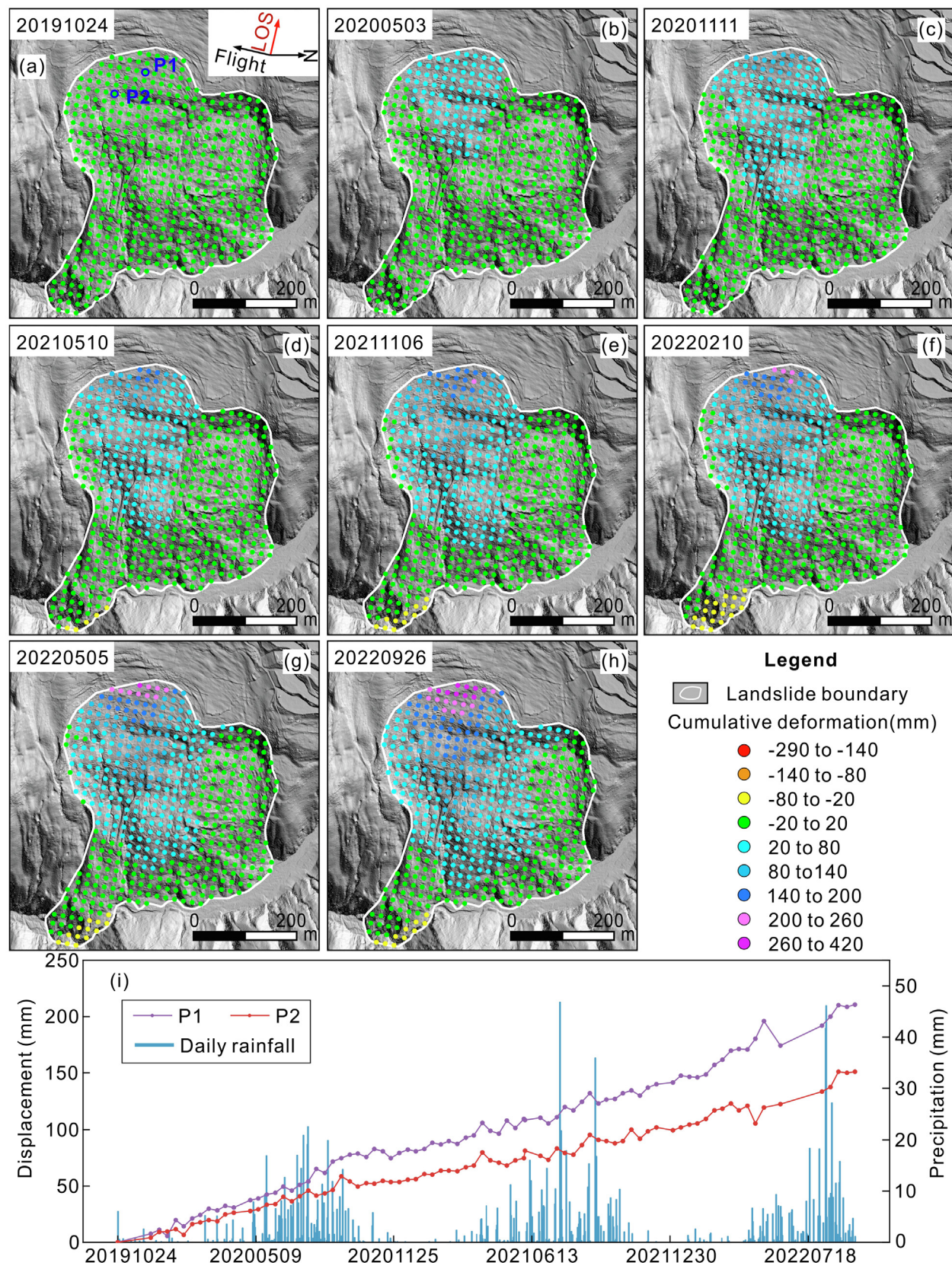


Fig. 9. Cumulative deformation at landslide L2 in the LOS direction between October 2019 and July 2022. P1-P2 in (a-h) are monitoring locations. (i) Time-series of daily rainfall and cumulative deformation at L2.

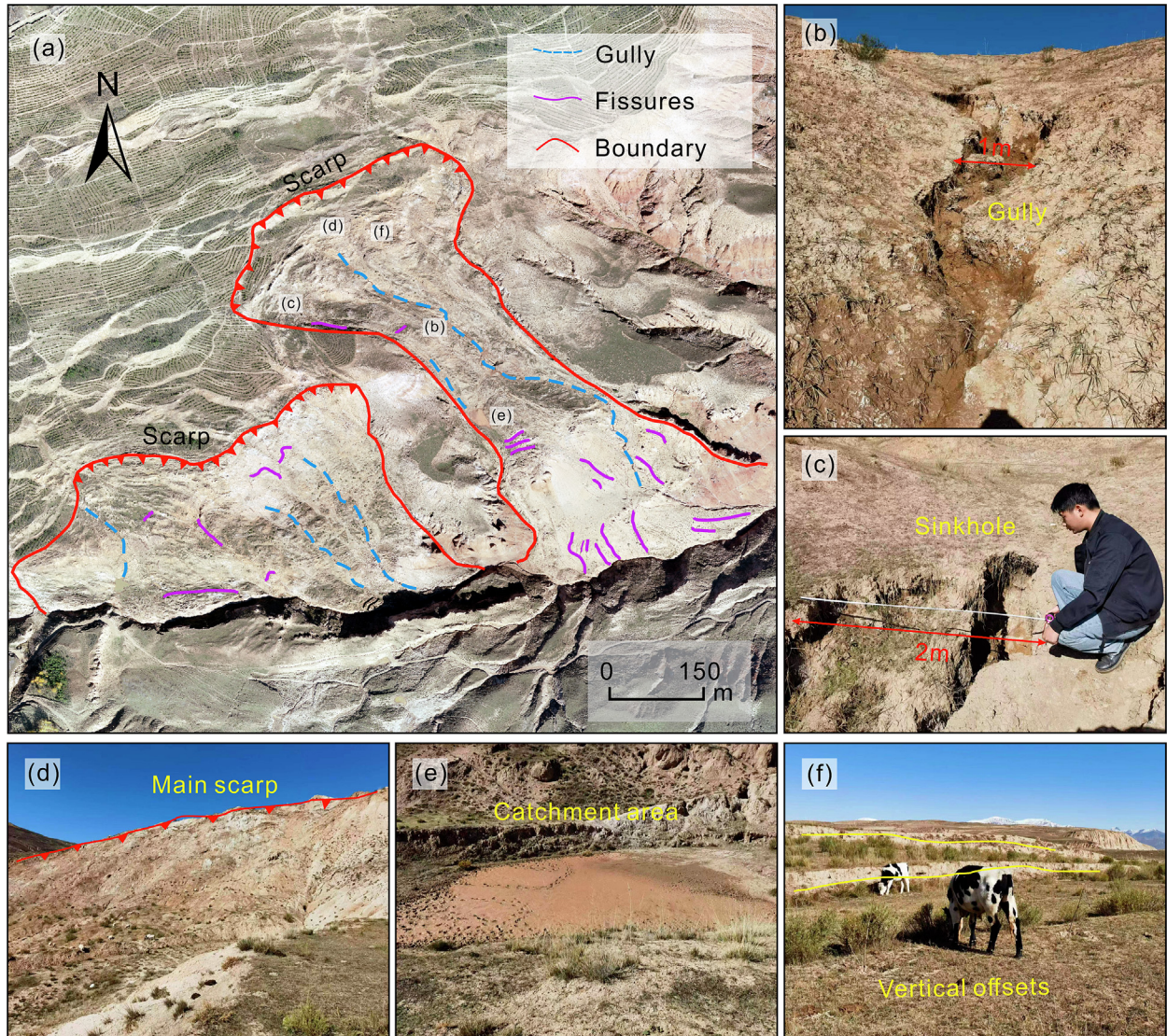


Fig. 10. Field investigation at landslides L3 and L4. (a) UAV panoramic view. (b) Gully. (c) Sinkhole. (d) Main scarp. (e) Catchment area. (f) Stepped landslide surface with vertical offsets.

5.2. Differences in dynamic susceptibility assessments

An effective dynamic susceptibility mapping method should produce reliable results. Presently, this approach often integrates InSAR technology and methods such as weighted superposition (Miao et al., 2023), dynamic factor (Liu et al., 2023a) and matrix (Shen et al., 2019). The weighted superposition method usually chooses numerical specific gravity based on regional environmental conditions and assigns it to both susceptibility assessment results and InSAR results to establish a dynamic susceptibility evaluation model (Liu et al., 2022a). However, the method has difficulties in accurately quantifying and selecting appropriate weight ratios, and it is challenging to apply it to other regions. The dynamic factor method uses the deformation rate of InSAR technology inversion as a dynamic evaluation input of the assessment model, but preparing the training set is time-consuming (Zhang et al., 2023). Moreover, these integrative methods often adopt one assessment model or select the best performance model from

several models, which might produce results that ignore the effects of randomness. All three of our models improved when combined with InSAR technology, which further avoided contingency and confirmed the validity of the coupled results.

The evaluation matrix method can quickly reflect changes in landslide susceptibility mapping without the need for time-consuming and expensive dynamic data modeling and analysis (Fang et al., 2022a). Furthermore, verifying the occurrence of landslides in areas of higher susceptibility by using remote sensing images alone is challenging, for these areas may also be unstable slopes caused by human activities. The here presented approach overcomes the limitations of previous landslide susceptibility verification methods that use remote sensing images by combining the quantitative evaluation of confusion matrix, the qualitative evaluation of UAV and satellite imagery, field surveys, and other diversified methods. Assessment results reflect on susceptibility changes caused by the deformation rate, and more effectively confirm the reasons for deformation variety.

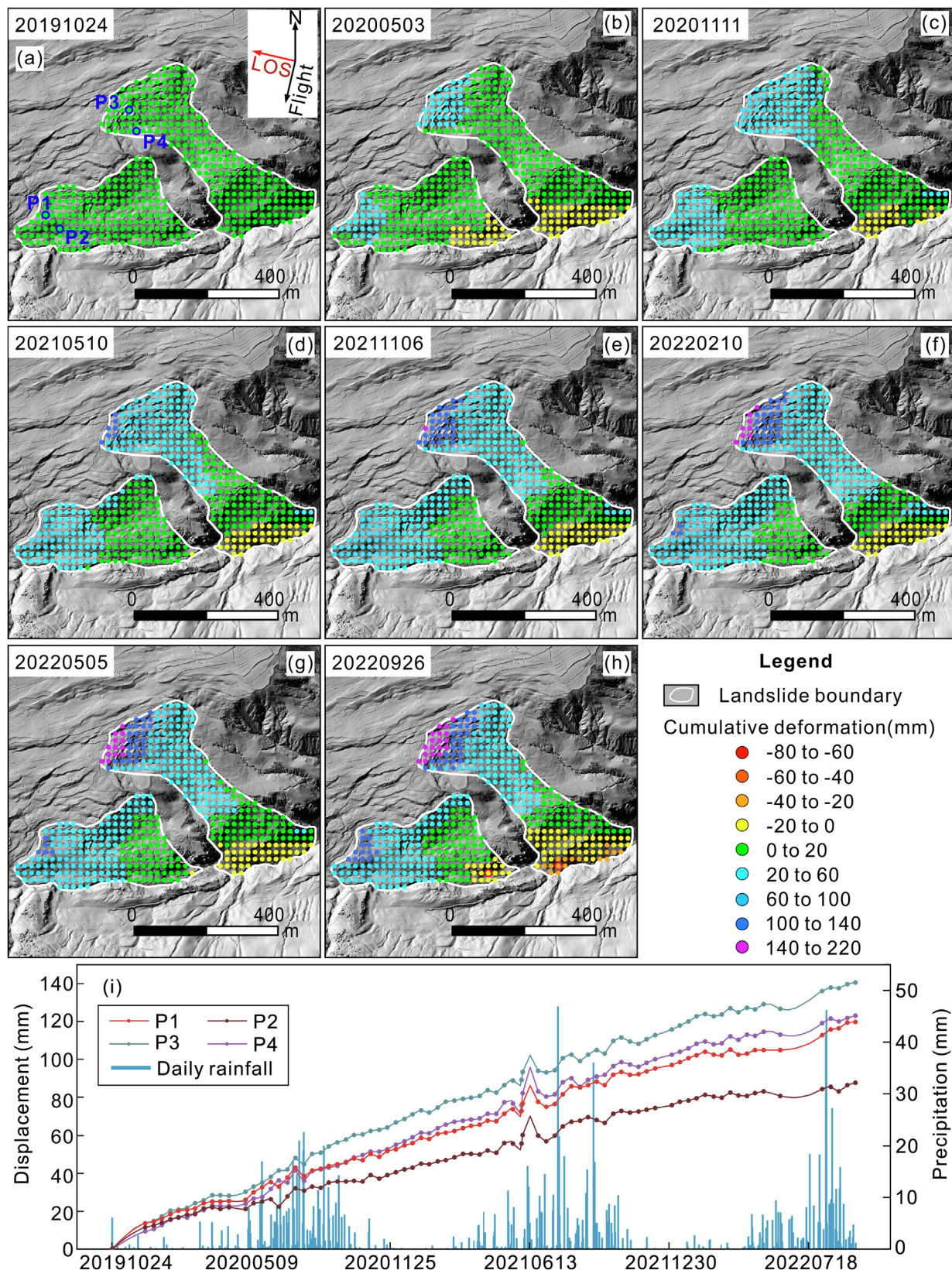


Fig. 11. Cumulative deformation at landslides L3 and L4 in the LOS direction between October 2019 and July 2022. P1-P4 in (a-h) are monitoring locations. (i) Time-series of daily rainfall and cumulative deformation at L3 (P1 + 2) and L4 (P3 + 4).

5.3. Existing deficiencies and outlook

The degree of improvement in the predictive ability of our approach may be affected by the selected landslide susceptibility assessment models, environment conditions, and the inherent limitations of InSAR technology. Specifically, different study areas have varying adaptability to different evaluation models due to differing environments, but there is neither a standard nor an optimal evaluation model in landslide susceptibility research (He et al., 2019; Zhao et al., 2021b). Atmospheric and vegetation interferences are difficult to thoroughly eliminate during InSAR processing, which may increase systematic errors (Wasowski and Bovenga, 2014; Zhao et al., 2021a). Hence, subsequent studies aim to further develop corresponding algorithms that minimize effects of atmosphere and vegetation (Zhu et al., 2023). Further research can attempt to combine InSAR with more advanced evaluation models, for example, some emerging AI models (Wang et al., 2024) that provide development opportunities for improving the predictive ability of coupled models and a better display of results. Although these limitations may be crucial in some cases, their impact on the main findings and conclusions is limited when considering the objectives of this study.

6. Conclusions

This study explored a landslide susceptibility assessment that integrates InSAR technology and machine learning models and revealed the feasibility of InSAR technology in updating preliminary susceptibility mapping results. It also investigated differences in susceptibility mapping results using combinations of methods. The results show that our coupled model can more accurately assess dynamic changes in landslide susceptibility and improve traditional landslide susceptibility assessment. Compared with the RF-InSAR and GBDT-InSAR models, the LR-InSAR model produced the best results as it detected areas of high and very high landslide susceptibility. As such, our approach achieved a refined analysis of landslide susceptibility. Dynamic assessment methods are a powerful tool in supporting regional landslide management and hazard mitigation strategies.

CRediT authorship contribution statement

Yingdong Wei: Writing – original draft, Visualization, Methodology, Formal analysis. **Haijun Qiu:** Writing – review & editing, Supervision, Project administration, Funding acquisition, Conceptualization. **Zijing Liu:** Methodology, Investigation. **Wencho Huangfu:** Validation, Resources. **Yaru Zhu:** Resources, Data curation. **Ya Liu:** Resources, Methodology. **Dongdong Yang:** Visualization, Validation. **Ulrich Kamp:** Writing – review & editing, Formal analysis.

Declaration of competing interest

The authors declare that they have no known competing financial interests or personal relationships that could have appeared to influence the work reported in this paper.

Acknowledgments

This work was funded by the National Natural Science Foundation of China (Grant No. 42271078), and Key Research and Development Program of Shaanxi (2024SF-YBXM-669).

References

- Al-Abadi, A.M., Al-Najar, N.A., 2019. Comparative assessment of bivariate, multivariate and machine learning models for mapping flood proneness. *Nat. Hazards* 100 (2), 461–491. <https://doi.org/10.1007/s11069-019-03821-y>.
- An, H., Viet, T.T., Lee, G., Kim, Y., Kim, M., Noh, S., Noh, J., 2016. Development of time-variant landslide-prediction software considering three-dimensional subsurface unsaturated flow. *Environ. Modell. Softw.* 85, 172–183. <https://doi.org/10.1016/j.envsoft.2016.08.009>.
- Arabameri, A., Saha, S., Roy, J., Chen, W., Blaschke, T., Tien Bui, D., 2020. Landslide susceptibility evaluation and management using different machine learning methods in The Gallicash River Watershed. *Iran. Remote Sens.* 12, 475. <https://doi.org/10.3390/rs12030475>.
- Ayalew, L., Yamagishi, H., 2005. The application of GIS-based logistic regression for landslide susceptibility mapping in the Kakuda-Yahiko Mountains Central Japan. *Geomorphology* 65 (1–2), 15–31. <https://doi.org/10.1016/j.geomorph.2004.06.010>.
- Baharvand, S., Rahnamarad, J., Soori, S., Saadatkhan, N., 2020. Landslide susceptibility zoning in a catchment of Zagros Mountains using fuzzy logic and GIS. *Environ. Earth Sci.* 79 (10), 1–10. <https://doi.org/10.1007/s12665-020-08957-w>.
- Berardino, P., Fornaro, G., Lanari, R., Sansosti, E., 2002. A new algorithm for surface deformation monitoring based on small baseline differential SAR interferograms. *IEEE Trans. Geosci. Remote Sensing* 40 (11), 2375–2383. <https://doi.org/10.1109/tgrs.2002.803792>.
- Breiman, L., 2001. *Random forests. Mach. Learn.* 45 (1), 5–32.
- Cao, C., Zhu, K., Xu, P., Shan, B., Yang, G., Song, S., 2022. Refined landslide susceptibility analysis based on InSAR technology and UAV multi-source data. *J. Clean. Prod.* 368, 133146. <https://doi.org/10.1016/j.jclepro.2022.133146>.
- Chang, Z., Huang, F., Huang, J., Jiang, S.H., Liu, Y., Meena, S.R., Catani, F., 2023. An updating of landslide susceptibility prediction from the perspective of space and time. *Geosci. Front.* 14 (5), 101619. <https://doi.org/10.1016/j.gsf.2023.101619>.
- Ciampalini, A., Raspini, F., Lagomarsino, D., Catani, F., Casagli, N., 2016. Landslide susceptibility map refinement using PSInSAR data. *Remote Sens. Environ.* 184, 302–315. <https://doi.org/10.1016/j.rse.2016.07.018>.
- Crosetto, M., Monserrat, O., Cuevas-González, M., Devanthéry, N., Crippa, B., 2016. Persistent Scatterer Interferometry: A review. *ISPRS-J. Photogramm. Remote Sens.* 115, 78–89. <https://doi.org/10.1016/j.isprsjprs.2015.10.011>.
- Dai, K., Chen, C., Shi, X., Wu, M., Feng, W., Xu, Q., Liang, R., Zhuo, G., Li, Z., 2023b. Dynamic landslides susceptibility evaluation in Baihetan Dam area during extensive impoundment by integrating geological model and InSAR observations. *Int. J. Appl. Earth Obs. Geoinf.* 116, 103157. <https://doi.org/10.1016/j.jag.2022.103157>.
- Dai, C., Li, W., Lu, H., Zhang, S., 2023a. Landslide Hazard Assessment Method Considering the Deformation Factor: A Case Study of Zhouqu, Gansu Province Northwest China. *Remote Sens.* 15 (3), 596. <https://doi.org/10.3390/rs15030596>.
- Devara, M., Tiwari, A., Dwivedi, R., 2021. Landslide susceptibility mapping using MT-InSAR and AHP enabled GIS-based multi-criteria decision analysis. *Geomat. Nat. Hazards Risk* 12 (1), 675–693. <https://doi.org/10.1080/1945705.2021.1887939>.
- Dong, J., Liao, M., Xu, Q., Zhang, L., Tang, M., Gong, J., 2018. Detection and displacement characterization of landslides using multi-temporal satellite SAR interferometry: A case study of Danba County in the Dadu River Basin. *Eng. Geol.* 240, 95–109. <https://doi.org/10.1016/j.enggeo.2018.04.015>.
- Dou, J., Yunus, A.P., Tien Bui, D., Merghadi, A., Sahana, M., Zhu, Z., Chen, C.W., Khosravi, K., Yang, Y., Pham, B.T., 2019. Assessment of advanced random forest and decision tree algorithms for modeling rainfall-induced landslide susceptibility in the Izu-Oshima Volcanic Island. *Japan. Sci. Total Environ.* 662, 332–346. <https://doi.org/10.1016/j.scitotenv.2019.01.221>.
- Du, J., Li, Z., Song, C., Zhu, W., Ji, Y., Zhang, C., Chen, B., Su, S., 2023. InSAR-Based Active Landslide Detection and Characterization Along the Upper Reaches of the Yellow River. *IEEE J. Sel. Top. Appl. Earth Observ. Remote Sens.* 16, 3819–3830. <https://doi.org/10.1109/jstars.2023.3263003>.
- Fang, H., Shao, Y., Xie, C., Tian, B., Zhu, Y., Guo, Y., Yang, Q., Yang, Y., 2022a. Using Persistent Scatterer Interferometry for Post-Earthquake Landslide Susceptibility Mapping in Jiuzhaigou. *Appl. Sci.-Basel.* 12 (18), 9228. <https://doi.org/10.3390/app12189228>.
- Fang, Z., Wang, Y., Duan, H., Niu, R., Peng, L., 2022b. Comparison of general kernel, multiple kernel, infinite ensemble and semi-supervised support vector machines for landslide susceptibility prediction. *Stoch. Environ. Res. Risk Assess.* 36 (10), 3535–3556. <https://doi.org/10.1007/s00477-022-02208-z>.
- Fell, R., Corominas, J., Bonnard, C., Cascini, L., Leroi, E., Savage, W.Z., 2008. Guidelines for landslide susceptibility, hazard and risk zoning for land use planning. *Eng. Geol.* 102 (3–4), 85–98. <https://doi.org/10.1016/j.enggeo.2008.03.009>.
- Ferretti, A., Prati, C., Rocca, F., 2001. Permanent scatterers in SAR interferometry. *IEEE Trans. Geosci. Remote Sensing* 39 (1), 8–20. <https://doi.org/10.1109/36.898661>.
- Frattini, P., Crosta, G., Carrara, A., 2010. Techniques for evaluating the performance of landslide susceptibility models. *Eng. Geol.* 111 (1–4), 62–72. <https://doi.org/10.1016/j.enggeo.2009.09.001>.

- [10.1016/j.enggeo.2009.12.004](https://doi.org/10.1016/j.enggeo.2009.12.004).
- Friedman, J.H., 2001. Greedy function approximation: A gradient boosting machine. *Ann. Stat.* 29 (5), 1189–1232. <https://doi.org/10.1214/aos/1013203451>.
- Froude, M.J., Petley, D.N., 2018. Global fatal landslide occurrence from 2004 to 2016. *Nat. Hazards Earth Syst. Sci.* 18 (8), 2161–2181. <https://doi.org/10.5194/nhess-18-2161-2018>.
- Fu, Z., Li, C., Yao, W., 2023. Landslide susceptibility assessment through TrAdaBoost transfer learning models using two landslide inventories. *Catena* 222, 106799. <https://doi.org/10.1016/j.catena.2022.106799>.
- Gantimurova, S., Parshin, A., Erofeev, V., 2021. GIS-Based Landslide Susceptibility Mapping of the Circum-Baikal Railway in Russia Using UAV Data. *Remote Sens.* 13 (18), 3629. <https://doi.org/10.3390/rs13183629>.
- Gariano, S.L., Guzzetti, F., 2016. Landslides in a changing climate. *Earth Sci. Rev.* 162, 227–252. <https://doi.org/10.1016/j.earscirev.2016.08.011>.
- Gupta, S.K., Shukla, D.P., 2023. Handling data imbalance in machine learning based landslide susceptibility mapping: a case study of Mandakini River Basin North-Western Himalayas. *Landslides* 20 (5), 933–949. <https://doi.org/10.1007/s10346-022-01998-1>.
- He, Q., Shahabi, H., Shirzadi, A., Li, S., Chen, W., Wang, N., Chai, H., Bian, H., Ma, J., Chen, Y., Wang, X., Chapi, K., Ahmad, B.B., 2019. Landslide spatial modelling using novel bivariate statistical based Naïve Bayes, RBF Classifier, and RBF Network machine learning algorithms. *Sci. Total Environ.* 663, 1–15. <https://doi.org/10.1016/j.scitotenv.2019.01.329>.
- Hong, H., 2023. Assessing landslide susceptibility based on hybrid Best-first decision tree with ensemble learning model. *Ecol. Ind.* 147, 109968. <https://doi.org/10.1016/j.ecolind.2023.109968>.
- Hooper, A., 2008. A multi-temporal InSAR method incorporating both persistent scatterer and small baseline approaches. *Geophys. Res. Lett.* 35 (16), L16302. <https://doi.org/10.1029/2008gl034654>.
- Huang, F., Cao, Z., Guo, J., Jiang, S.H., Li, S., Guo, Z., 2020. Comparisons of heuristic, general statistical and machine learning models for landslide susceptibility prediction and mapping. *Catena* 191, 104580. <https://doi.org/10.1016/j.catena.2020.104580>.
- Huang, F., Yan, J., Fan, X., Yao, C., Huang, J., Chen, W., Hong, H., 2022. Uncertainty pattern in landslide susceptibility prediction modelling: Effects of different landslide boundaries and spatial shape expressions. *Geosci. Front.* 13 (2), 101317. <https://doi.org/10.1016/j.gsf.2021.101317>.
- Hussain, S., Hongxing, S., Ali, M., Ali, M., 2021. PS-InSAR based validated landslide susceptibility modelling: a case study of Ghizer valley, Northern Pakistan. *Geocarto Int.* 37 (13), 3941–3962. <https://doi.org/10.1080/10106049.2020.1870165>.
- Jenks, G.F., 1967. The data model concept in statistical mapping. *Int. Yearb. Cartogr.* 7, 186–190.
- Jiang, Z., Wang, M., Liu, K., 2023. Comparisons of Convolutional Neural Network and Other Machine Learning Methods in Landslide Susceptibility Assessment: A Case Study in Pingwu. *Remote Sens.* 15 (3), 798. <https://doi.org/10.3390/rs15030798>.
- Kohestani, V.R., Hassanlourad, M., Ardakani, A., 2015. Evaluation of liquefaction potential based on CPT data using random forest. *Nat. Hazards* 79 (2), 1079–1089. <https://doi.org/10.1007/s11069-015-1893-5>.
- Kumar, C., Walton, G., Santi, P., Luza, C., 2023. An Ensemble Approach of Feature Selection and Machine Learning Models for Regional Landslide Susceptibility Mapping in the Arid Mountainous Terrain of Southern Peru. *Remote Sens.* 15 (5), 1376. <https://doi.org/10.3390/rs15051376>.
- Li, Y., Hong, H., 2023. Modelling flood susceptibility based on deep learning coupling with ensemble learning models. *J. Environ. Manage.* 325, 116450. <https://doi.org/10.1016/j.jenvman.2022.116450>.
- Li, M., Zhang, L., Ding, C., Li, W., Luo, H., Liao, M., Xu, Q., 2020. Retrieval of historical surface displacements of the Baige landslide from time-series SAR observations for retrospective analysis of the collapse event. *Remote Sens. Environ.* 240, 111695. <https://doi.org/10.1016/j.rse.2020.111695>.
- Liang, Z., Wang, C., Duan, Z., Liu, H., Liu, X., Khan, U.J., K., 2021. A Hybrid Model Consisting of Supervised and Unsupervised Learning for Landslide Susceptibility Mapping. *Remote Sens.* 13 (8), 1464. <https://doi.org/10.3390/rs13081464>.
- Liu, Q., Tang, A., Huang, D., 2023b. Exploring the uncertainty of landslide susceptibility assessment caused by the number of non-landslides. *Catena* 227, 107109. <https://doi.org/10.1016/j.catena.2023.107109>.
- Liu, S., Wang, L., Zhang, W., Sun, W., Fu, J., Xiao, T., Dai, Z., 2023c. A physics-informed data-driven model for landslide susceptibility assessment in the Three Gorges Reservoir area. *Geosci. Front.* 14 (5), 101621. <https://doi.org/10.1016/j.gsf.2023.101621>.
- Liu, M., Xu, B., Li, Z., Mao, W., Zhu, Y., Hou, J., Liu, W., 2023a. Landslide Susceptibility Zoning in Yunnan Province Based on SBAS-InSAR Technology and a Random Forest Model. *Remote Sens.* 15 (11), 2864. <https://doi.org/10.3390/rs15122864>.
- Liu, W., Zhang, Y., Liang, Y., Sun, P., Li, Y., Su, X., Wang, A., Meng, X., 2022a. Landslide Risk Assessment Using a Combined Approach Based on InSAR and Random Forest. *Remote Sens.* 14 (9), 2131. <https://doi.org/10.3390/rs14092131>.
- Liu, Y., Zhao, L., Bao, A., Li, J., Yan, X., 2022b. Chinese High Resolution Satellite Data and GIS-Based Assessment of Landslide Susceptibility along Highway G30 in Guozigou Valley Using Logistic Regression and MaxEnt Model. *Remote Sens.* 14 (15), 3620. <https://doi.org/10.3390/rs14153620>.
- Liu, Y., Qiu, H., Kamp, U., Wang, N., Wang, J., Huang, C., Tang, B., 2024. Higher temperature sensitivity of retrogressive thaw slump activity in the Arctic compared to the Third Pole. *Sci. Total Environ.* 914, 170007. <https://doi.org/10.1016/j.scitotenv.2024.170007>.
- Ma, P., Wang, W., Zhang, B., Wang, J., Shi, G., Huang, G., Chen, F., Jiang, L., Lin, H., 2019. Remotely sensing large- and small-scale ground subsidence: A case study of the Guangdong-Hong Kong-Macao Greater Bay Area of China. *Remote Sens. Environ.* 232, 111282. <https://doi.org/10.1016/j.rse.2019.111282>.
- Ma, P., Cui, Y., Wang, W., Lin, H., Zhang, Y., 2021. Coupling InSAR and numerical modeling for characterizing landslide movements under complex loads in urbanized hillslopes. *Landslides* 18 (5), 1611–1623. <https://doi.org/10.1007/s10346-020-01604-2>.
- Ma, S., Qiu, H., Zhu, Y., Yang, D., Tang, B., Wang, D., Wang, L., Cao, M., 2023. Topographic Changes, Surface Deformation and Movement Process before, during and after a Rotational Landslide. *Remote Sens.* 15 (3), 662. <https://doi.org/10.3390/rs15030662>.
- Medina, V., Hürlimann, M., Guo, Z., Lloret, A., Vaunat, J., 2021. Fast physically-based model for rainfall-induced landslide susceptibility assessment at regional scale. *Catena* 201, 105213. <https://doi.org/10.1016/j.catena.2021.105213>.
- Miao, F., Ruan, Q., Wu, Y., Qian, Z., Kong, Z., Qin, Z., 2023. Landslide Dynamic Susceptibility Mapping Base on Machine Learning and the PS-InSAR Coupling Model. *Remote Sens.* 15 (22), 5427. <https://doi.org/10.3390/rs15225427>.
- Morishita, Y., Lazecky, M., Wright, T., Weiss, J., Elliott, J., Hooper, A., 2020. LiCSBAS: An Open-Source InSAR Time Series Analysis Package Integrated with the LiCSAR Automated Sentinel-1 InSAR Processor. *Remote Sens.* 12 (3), 424. <https://doi.org/10.3390/rs12030424>.
- Novellino, A., Cesarano, M., Cappelletti, P., Di Martire, D., Di Napoli, M., Ramondini, M., Sowter, A., Calcaterra, D., 2021. Slow-moving landslide risk assessment combining Machine Learning and InSAR techniques. *Catena* 203, 105317. <https://doi.org/10.1016/j.catena.2021.105317>.
- Noviello, C., Verde, S., Zamparelli, V., Fornaro, G., Paucillo, A., Reale, D., Nicodemo, G., Ferlisi, S., Gulla, G., Peduto, D., 2020. Monitoring Buildings at Landslide Risk With SAR: A Methodology Based on the Use of Multipass Interferometric Data. *IEEE Geosci. Remote Sens. Mag.* 8 (1), 91–119. <https://doi.org/10.1109/mgrs.2019.2963140>.
- Pawluszek, K., Borkowski, A., 2017. Impact of DEM-derived factors and analytical hierarchy process on landslide susceptibility mapping in the region of Roźnow Lake, Poland. *Nat. Hazards* 86 (2), 919–952. <https://doi.org/10.1007/s11069-016-2725-y>.
- Petley, D., 2012. Global patterns of loss of life from landslides. *Geology* 40 (10), 927–930. <https://doi.org/10.1130/g33217.1>.
- Pham, B.T., Shirzadi, A., Tien Bui, D., Prakash, I., Dholakia, M., 2018. A hybrid machine learning ensemble approach based on a Radial Basis Function neural network and Rotation Forest for landslide susceptibility modeling: A case study in the Himalayan area, India. *Int. J. Sediment Res.* 33 (2), 157–170. <https://doi.org/10.1016/j.ijscr.2017.09.008>.
- Qiu, H., Su, L., Tang, B., Yang, D., Ullah, M., Zhu, Y., Kamp, U., 2024. The effect of location and geometric properties of landslides caused by rainstorms and earthquakes. *Earth Surf. Proc. Land.* 1–13. <https://doi.org/10.1002/esp.5816>.
- Raucoules, D., de Michele, M., Malet, J.P., Ulrich, P., 2013. Time-variable 3D ground displacements from high-resolution synthetic aperture radar (SAR) application to La Valette landslide (South French Alps). *Remote Sens. Environ.* 139, 198–204. <https://doi.org/10.1016/j.rse.2013.08.006>.
- Reichenbach, P., Rossi, M., Malamud, B.D., Mihir, M., Guzzetti, F., 2018. A review of statistically-based landslide susceptibility models. *Earth Sci. Rev.* 180, 60–91. <https://doi.org/10.1016/j.earscirev.2018.03.001>.
- Ren, T., Gao, L., Gong, W., 2023. An ensemble of dynamic rainfall index and machine learning method for spatiotemporal landslide susceptibility modeling. *Landslides* 21 (2), 257–273. <https://doi.org/10.1007/s10346-023-02152-1>.
- Shahzad, N., Ding, X., Wu, S., Liang, H., 2020. Ground Deformation and Its Causes in Abbottabad City, Pakistan from Sentinel-1A Data and MT-InSAR. *Remote Sens.* 12 (20), 3442. <https://doi.org/10.3390/rs1203442>.
- Shan, Y., Xu, Z., Zhou, S., Lu, H., Yu, W., Li, Z., Cao, X., Li, P., Li, W., 2023. Landslide Hazard Assessment Combined with InSAR Deformation: A Case Study in the Zagunao River Basin, Sichuan Province Southwestern China. *Remote Sens.* 16 (1), 99. <https://doi.org/10.3390/rs16010099>.
- Sharma, N., Saharia, M., Ramana, G., 2024. High resolution landslide susceptibility mapping using ensemble machine learning and geospatial big data. *Catena* 235, 107653. <https://doi.org/10.1016/j.catena.2023.107653>.
- Shen, C., Feng, Z., Xie, C., Fang, H., Zhao, B., Ou, W., Zhu, Y., Wang, K., Li, H., Bai, H., Mannan, A., Chen, P., 2019. Refinement of Landslide Susceptibility Map Using Persistent Scatterer Interferometry in Areas of Intense Mining Activities in the Karst Region of Southwest China. *Remote Sens.* 11 (23), 2821. <https://doi.org/10.3390/rs11232821>.
- Shi, X., Yang, C., Zhang, L., Jiang, H., Liao, M., Zhang, L., Liu, X., 2019. Mapping and characterizing displacements of active loess slopes along the upstream Yellow River with multi-temporal InSAR datasets. *Sci. Total Environ.* 674, 200–210. <https://doi.org/10.1016/j.scitotenv.2019.04.140>.
- Solari, L., Bianchini, S., Franceschini, R., Barra, A., Monserrat, O., Thuegaz, P., Bertolo, D., Crosetto, M., Catani, F., 2020. Satellite interferometric data for landslide intensity evaluation in mountainous regions. *Int. J. Appl. Earth Obs. Geoinf.* 87, 102028. <https://doi.org/10.1016/j.jag.2019.102028>.
- Steger, S., Mair, V., Kofler, C., Pittore, M., Zebisch, M., Schneiderbauer, S., 2021. Correlation does not imply geomorphic causation in data-driven landslide susceptibility modelling—Benefits of exploring landslide data collection effects. *Sci. Total Environ.* 776, 145935. <https://doi.org/10.1016/j.scitotenv.2021.145935>.
- Sun, H., Li, W., Scaioni, M., Fu, J., Guo, X., Gao, J., 2023. Influence of spatial heterogeneity on landslide susceptibility in the transboundary area of the

- Himalayas. *Geomorphology* 433, 108723. <https://doi.org/10.1016/j.geomorph.2023.108723>.
- Wang, Y., Fang, Z., Wang, M., Peng, L., Hong, H., 2020b. Comparative study of landslide susceptibility mapping with different recurrent neural networks. *Comput. Geosci.* 138, 104445. <https://doi.org/10.1016/j.cageo.2020.104445>.
- Wang, L., Wu, C., Tang, L., Zhang, W., Lacasse, S., Liu, H., Gao, L., 2020a. Efficient reliability analysis of earth dam slope stability using extreme gradient boosting method. *Acta Geotech.* 15 (11), 3135–3150. <https://doi.org/10.1007/s11440-020-00962-4>.
- Wang, N., Zhang, H., Dahal, A., Cheng, W., Zhao, M., Lombardo, L., 2024. On the use of explainable AI for susceptibility modeling: Examining the spatial pattern of SHAP values. *Geosci. Front.* 15 (4), 101800. <https://doi.org/10.1016/j.gsf.2024.101800>.
- Wasowski, J., Bovenga, F., 2014. Investigating landslides and unstable slopes with satellite Multi Temporal Interferometry: Current issues and future perspectives. *Eng. Geol.* 174, 103–138. <https://doi.org/10.1016/j.enggeo.2014.03.003>.
- Xie, Z., Chen, G., Meng, X., Zhang, Y., Qiao, L., Tan, L., 2017. A comparative study of landslide susceptibility mapping using weight of evidence, logistic regression and support vector machine and evaluated by SBAS-InSAR monitoring: Zhouou to Wudu segment in Bailong River Basin China. *Environ. Earth Sci.* 76 (8), 1–19. <https://doi.org/10.1007/s12665-017-6640-7>.
- Yang, D., Qiu, H., Ye, B., Liu, Y., Zhang, J., Zhu, Y., 2023a. Distribution and Recurrence of Warming-Induced Retrogressive Thaw Slumps on the Central Qinghai-Tibet Plateau e2022JF007047. *J. Geophys. Res. Earth Surf.* 128 (8). <https://doi.org/10.1029/2022jf007047>.
- Yang, H., Song, K., Chen, L., Qu, L., 2023b. Hysteresis effect and seasonal step-like creep deformation of the Jiuxianping landslide in the Three Gorges Reservoir region. *Eng. Geol.* 317, 107089. <https://doi.org/10.1016/j.enggeo.2023.107089>.
- Yao, Z., Chen, M., Zhan, J., Zhuang, J., Sun, Y., Yu, Q., Yu, Z., 2023b. Refined Landslide Susceptibility Mapping by Integrating the SHAP-CatBoost Model and InSAR Observations: A Case Study of Lishui, Southern China. *Appl. Sci.-Basel.* 13 (23), 12817. <https://doi.org/10.3390/app132312817>.
- Yao, T., Thompson, L., Yang, W., Yu, W., Gao, Y., Guo, X., Yang, X., Duan, K., Zhao, H., Xu, B., Pu, J., Lu, A., Xiang, Y., Kattel, D.B., Joswiak, D., 2012. Different glacier status with atmospheric circulations in Tibetan Plateau and surroundings. *Nat. Clim. Chang.* 2 (9), 663–667. <https://doi.org/10.1038/nclimate1580>.
- Yao, J., Yao, X., Zhao, Z., Liu, X., 2023a. Performance comparison of landslide susceptibility mapping under multiple machine-learning based models considering InSAR deformation: a case study of the upper Jinsha River. *Geomat. Nat. Hazards Risk* 14 (1), 2212833. <https://doi.org/10.1080/19475705.2023.2212833>.
- Ye, B., Qiu, H., Tang, B., Liu, Y., Liu, Z., Jiang, X., Yang, D., Ullah, M., Zhu, Y., Kamp, U., 2024. Creep deformation monitoring of landslides in a reservoir area. *J. Hydrol.* 632, 130905. <https://doi.org/10.1016/j.jhydrol.2024.130905>.
- Yi, Y., Zhang, Z., Zhang, W., Jia, H., Zhang, J., 2020. Landslide susceptibility mapping using multiscale sampling strategy and convolutional neural network: A case study in Jiuzhaigou region. *Catena* 195, 104851. <https://doi.org/10.1016/j.catena.2020.104851>.
- Youssef, A.M., Pourghasemi, H.R., Pourtaghi, Z.S., Al-Katheeri, M.M., 2015. Landslide susceptibility mapping using random forest, boosted regression tree, classification and regression tree, and general linear models and comparison of their performance at Wadi Tayyah Basin, Asir Region, Saudi Arabia. *Landslides* 13 (5), 839–856. <https://doi.org/10.1007/s10346-015-0614-1>.
- Youssef, K., Shao, K., Moon, S., Bouchard, L.S., 2023. Landslide susceptibility modeling by interpretable neural network. *Commun. Earth Environ.* 4 (1), 162. <https://doi.org/10.1038/s43247-023-00806-5>.
- Zhang, W., Liu, S., Wang, L., Samui, P., Chwala, M., He, Y., 2022a. Landslide Susceptibility Research Combining Qualitative Analysis and Quantitative Evaluation: A Case Study of Yunyang County in Chongqing China. *Forests* 13 (7), 1055. <https://doi.org/10.3390/f13071055>.
- Zhang, W., Li, H., Han, L., Chen, L., Wang, L., 2022b. Slope stability prediction using ensemble learning techniques: A case study in Yunyang County, Chongqing China. *J. Rock Mech. Geotech. Eng.* 14 (4), 1089–1099. <https://doi.org/10.1016/j.jrmge.2021.12.011>.
- Zhang, G., Wang, S., Chen, Z., Liu, Y., Xu, Z., Zhao, R., 2023. Landslide susceptibility evaluation integrating weight of evidence model and InSAR results, west of Hubei Province, China. *Egypt. J. Remote Sens. Space Sci.* 26 (1), 95–106. <https://doi.org/10.1016/j.ejrs.2022.12.010>.
- Zhang, W., Wu, C., Zhong, H., Li, Y., Wang, L., 2021. Prediction of undrained shear strength using extreme gradient boosting and random forest based on Bayesian optimization. *Geosci. Front.* 12 (1), 469–477. <https://doi.org/10.1016/j.gsf.2020.03.007>.
- Zhao, Z., Chen, J., Xu, K., Xie, H., Gan, X., Xu, H., 2021b. A spatial case-based reasoning method for regional landslide risk assessment. *Int. J. Appl. Earth Obs. Geoinf.* 102, 102381. <https://doi.org/10.1016/j.jag.2021.102381>.
- Zhao, Z., Chen, J., Yao, J., Xu, K., Liao, Y., Xie, H., Gan, X., 2023. An improved spatial case-based reasoning considering multiple spatial drivers of geographic events and its application in landslide susceptibility mapping. *Catena* 223, 106940. <https://doi.org/10.1016/j.catena.2023.106940>.
- Zhao, L., Liang, R., Shi, X., Dai, K., Cheng, J., Cao, J., 2021a. Detecting and Analyzing the Displacement of a Small-Magnitude Earthquake Cluster in Rong County, China by the GACOS Based InSAR Technology. *Remote Sens.* 13 (20), 4137. <https://doi.org/10.3390/rs13204137>.
- Zhou, C., Cao, Y., Hu, X., Yin, K., Wang, Y., Catani, F., 2022. Enhanced dynamic landslide hazard mapping using MT-InSAR method in the Three Gorges Reservoir Area. *Landslides* 19 (7), 1585–1597. <https://doi.org/10.1007/s10346-021-01796-1>.
- Zhu, Y., Qiu, H., Cui, P., Liu, Z., Ye, B., Yang, D., Kamp, U., 2023. Early detection of potential landslides along high-speed railway lines: A pressing issue. *Earth Surf. Proc. Land.* 48 (15), 3302–3314. <https://doi.org/10.1002/esp.5697>.